

## Article

# Facile Fabrication of Mixed-Cation $\text{FA}_{1-x}\text{Cs}_x\text{PbI}_3$ Perovskites Thin Films for Photodetector Applications

Fenyun Wang<sup>1</sup>, Pachaiyappan Murugan<sup>1</sup> , Shunhong Dong<sup>1</sup>, Xiaolu Zheng<sup>1</sup>, Jiaxiu Man<sup>1</sup>, Zhiyong Liu<sup>1,2</sup>, Weibin Zhang<sup>1,2</sup>, Ting Zhu<sup>1,2</sup>  and Hong-En Wang<sup>1,2,\*</sup>

<sup>1</sup> Yunnan Key Laboratory of Optoelectronic Information Technology, College of Physics and Electronic Information, Yunnan Normal University, Kunming 650500, China; p.kumu29@gmail.com (P.M.); shunhong.dong@outlook.com (S.D.); zhengxiaolu@ynnu.edu.cn (X.Z.); manjiaxiu@ynnu.edu.cn (J.M.); liuzhiyong@ynnu.edu.cn (Z.L.); 220001@ynnu.edu.cn (W.Z.); zhut0002@ynnu.edu.cn (T.Z.)

<sup>2</sup> Key Laboratory of Advanced Technique & Preparation for Renewable Energy Materials, Ministry of Education, Yunnan Normal University, Kunming 650500, China

\* Correspondence: honggen.wang@ynnu.edu.cn or honggen.wang@outlook.com

**Abstract:** Formamidinium lead triiodide (FAPbI<sub>3</sub>) perovskite has received great attention because of its distinct optoelectronic property, smaller band gap (~1.5 eV), and higher thermal stability than methylammonium lead triiodide (MAPbI<sub>3</sub>). However, the efficient synthesis of such perovskite materials on a large scale at a low cost remains a challenge. In this work, mixed-cation  $\text{FA}_{1-x}\text{Cs}_x\text{PbI}_3$  thin films were directly prepared in an atmospheric environment with a high film formation rate, low material loss, low cost, and low requirements for experimental instruments and environment. The as-obtained FAPbI<sub>3</sub> films exhibited excellent optoelectronic properties, showing promising applications in the photodetection field.

**Keywords:** mixed-cation  $\text{FA}_{1-x}\text{Cs}_x\text{PbI}_3$  thin film; perovskites; optoelectronic properties; photodetectors



**Citation:** Wang, F.; Murugan, P.; Dong, S.; Zheng, X.; Man, J.; Liu, Z.; Zhang, W.; Zhu, T.; Wang, H.-E. Facile Fabrication of Mixed-Cation  $\text{FA}_{1-x}\text{Cs}_x\text{PbI}_3$  Perovskites Thin Films for Photodetector Applications. *Photonics* **2023**, *10*, 312. <https://doi.org/10.3390/photonics10030312>

Received: 16 February 2023

Revised: 7 March 2023

Accepted: 11 March 2023

Published: 14 March 2023



**Copyright:** © 2023 by the authors. Licensee MDPI, Basel, Switzerland. This article is an open access article distributed under the terms and conditions of the Creative Commons Attribution (CC BY) license (<https://creativecommons.org/licenses/by/4.0/>).

## 1. Introduction

In recent years, organic–inorganic hybrid perovskite materials have attracted much attention in electronics and optoelectronic fields such as solar cells [1–3], light-emitting diodes [4,5], lasers [6], and photodetectors [7] due to their excellent optoelectronic properties. The device structure and mechanism of photodetectors have been widely studied. Specifically, the semiconductor material absorbs the incident light; generates photogenerated electrons/holes through the absorption and transit regions; and finally, the transmitted carriers are effectively collected to generate photocurrent. In particular, effective separation and collection of electron–hole pairs can only be achieved when the photon energy is greater than the semiconductor bandgap width ( $h\nu \geq E_g$ ). Compared with metal oxide semiconductors, metal nitrides, and 2D semiconductor materials, perovskites are widely used in optoelectronic devices due to their high light absorption coefficient, carrier mobility, and defect tolerance. In addition, perovskite materials can be synthesized by a simple solution method and integrated with other materials to form composites for better optoelectronic performances [8–11].

Generally, organometal halide perovskites adopt a chemical formula of  $\text{ABX}_3$ , where A is a monovalent cation ( $\text{CH}_3\text{NH}_3^+$ ,  $\text{CH}_2(\text{NH}_2)_2^+$ ,  $\text{Cs}^+$ , etc.), and B stands for  $\text{Pb}^{2+}$  or  $\text{Sn}^{2+}$ , while X is a halide anion ( $\text{Cl}^-$ ,  $\text{Br}^-$ , and  $\text{I}^-$ ). Early research mainly focused on methylammonium lead triiodide (MAPbI<sub>3</sub>). However, due to the volatile nature of MA [12], MAPbI<sub>3</sub> has poor environmental stability and is easily degraded under the conditions of oxygen, moisture, and high temperature [13]. These undesirable intrinsic attributes of MAPbI<sub>3</sub> largely impeded its wide application [14]. At present, the environmental stability of perovskite has been extensively studied. For example, Tai et al. [15] achieved a conversion efficiency of 15% based on proper humidity to promote the nucleation and

growth of perovskite. Moreover, Ivy M. et al. [16] combined the chemical synthesis method and solvent engineering technique to obtain pinhole-free thin-film perovskite composed of large crystalline grains and high crystalline quality. Sanjay et al. [17] used a one-step deposition technique, two-step deposition technique, and vapor deposition technique under the atmospheric atmosphere to obtain high crystalline quality, low defect density, and large-size perovskite thin film.

In comparison, black-phase formamidinium lead triiodide ( $\alpha$ -FAPbI<sub>3</sub>) exhibits relatively superior atmospheric stability with a slightly smaller bandgap (1.45~1.51 eV) more suitable for optoelectronic applications, which has become a major research avenue in the community [18,19]. Typically, FAPbI<sub>3</sub> can be prepared from organic and inorganic halide precursors by either a one-step or two-step method [20,21]. Snaith et al. reported the preparation of less uniform and flat  $\alpha$ -FAPbI<sub>3</sub> perovskite film by adding a certain amount of hydriodic acid (HI) [3]. Zhao et al. [22] introduced HPbI<sub>3</sub> into perovskite precursors and prepared relatively flat FAPbI<sub>3</sub> thin films by the one-step spin coating method. However, the as-prepared single FAPbI<sub>3</sub> films can still have many defects due to the larger FA<sup>+</sup> cation (2.53 Å) than that of MA<sup>+</sup> cation (2.17 Å) and the symmetry difference of FA<sup>+</sup> and MA<sup>+</sup> [23–25]. In addition, compared with MAPbI<sub>3</sub>,  $\alpha$ -FAPbI<sub>3</sub> is difficult to maintain its phase stability. Note that the phase stability/transition can be estimated by the Goldschmidt tolerance factor calculated from the ionic radius using the following expression [26]:

$$t = \frac{r_A + r_x}{\sqrt{2}(r_B + r_X)} \quad (1)$$

where  $r_A$  is the radius of the A-site cation,  $r_B$  is the radius of the B-site cation, and  $r_X$  is the radius of the anion. The calculated tolerance factor of FAPbI<sub>3</sub> is about 1, suggesting that it ideally has a (pseudo)cubic structure. When the default tolerance factor is higher than 1 or lower than 0.71, non-perovskite structures are formed [27].

Doping other cations or halide anions can improve the phase stability of FAPbI<sub>3</sub> [28]. For example, some cations (e.g., MA<sup>+</sup>, Cs<sup>+</sup>, Rb<sup>+</sup>, etc.) with an ionic radius smaller than FA<sup>+</sup> can be used to partially replace FA<sup>+</sup>. Among them, the intrinsically stable inorganic cation Cs<sup>+</sup> has a small ionic radius of 1.81 Å. By substituting part of FA<sup>+</sup> in pure FAPbI<sub>3</sub> with Cs<sup>+</sup>, the volume of the cuboctahedron motifs can be reduced so that metal cations and halogens can achieve stronger interaction to form highly crystalline perovskite materials. Himchan et al. [29] found that after doping Cs<sup>+</sup>, the resultant FA<sub>1-x</sub>Cs<sub>x</sub>PbBr<sub>3</sub> perovskite thin film underwent a lattice shrinkage as reflected by the shift of XRD diffraction peak position towards a larger angle direction. Therefore, by effectively adjusting the tolerance factor of the desired cubic structure, the expansion or contraction of the perovskite lattice can be achieved, and its crystal growth can be regulated. Based on previous reported work, Cs<sub>0.15</sub>FA<sub>0.85</sub>PbI<sub>3</sub> perovskite was nucleated and grown mostly in N<sub>2</sub> atmosphere (glove box). However, the lack of a proper humidity environment for Cs<sub>0.15</sub>FA<sub>0.85</sub>PbI<sub>3</sub> synthesis leads to the formation of high defect density, small size grains, and the increase in non-radiative complexes severely limits the application of perovskite optoelectronic devices [30]. Therefore, it is essential to develop a novel method (atmospheric atmosphere) for the preparation of Cs<sub>0.15</sub>FA<sub>0.85</sub>PbI<sub>3</sub> perovskite.

Nevertheless, due to the strong hygroscopic nature of FAI, most reported high-efficiency FAPbI<sub>3</sub> perovskites have been fabricated under some specific conditions, usually with the protection of inert gases such as Ar or N<sub>2</sub> in a glovebox [12]. Such synthetic routes can potentially increase the processing cost and difficulty of large-scale industrialization. Therefore, it is of great significance to explore a facile and low-cost method to prepare FAPbI<sub>3</sub> perovskite thin films on a large scale (the best is directly in an atmospheric environment). However, research in this area is still in its infancy. Herein, we report on the facile and fast fabrication of FA<sub>1-x</sub>Cs<sub>x</sub>PbI<sub>3</sub> thin films with tunable Cs<sup>+</sup> concentration (varied  $x$  values) in the atmosphere. The morphology, phase, microstructure, and composition of the as-prepared FA<sub>1-x</sub>Cs<sub>x</sub>PbI<sub>3</sub> thin films were carefully characterized. The results revealed that the optical properties of the as-prepared FA<sub>1-x</sub>Cs<sub>x</sub>PbI<sub>3</sub> thin films varied as a function

of the Cs<sup>+</sup> concentrations, and an excellent optical property can be achieved with a Cs<sup>+</sup> doping concentration of 15%. Further, the photodetection properties of the FA<sub>0.85</sub>Cs<sub>0.15</sub>PbI<sub>3</sub> thin film were investigated.

## 2. Experimental Section

### 2.1. Synthesis of Perovskite Precursor Solution

A 2 mol mL<sup>-1</sup> mixed solution was prepared by dissolving 0.461 g PbI<sub>2</sub> (Aldrich, Shanghai, China, 99.99%), as well as appropriate amounts of FAI (Aldrich, 99.5%) and CsI (Aldrich, 99.9%) powders with defined composition ratios, into 200 μL dimethyl sulfoxide (AR) and 800 μL N,N-dimethylformamide (AR), in that order. The resulting solution was heated in a water bath to 70 °C while being stirred for an hour, then cooled to room temperature before storage.

### 2.2. Preparation of FA<sub>1-x</sub>Cs<sub>x</sub>PbI<sub>3</sub> Thin Films

Squares of 1.5 cm × 1.5 cm were cut from a 4-inch SiO<sub>2</sub>/Si substrate (Zhejiang Lijing Optoelectronics Technology, Hangzhou, China). To make the SiO<sub>2</sub>/Si substrates more hydrophilic, they were sonicated in acetone, ethanol, and deionized water for 15 min in a squeegee, then dried with a nitrogen gun and treated with oxygen plasma for 10 min. The FA<sub>1-x</sub>Cs<sub>x</sub>PbI<sub>3</sub> thin films were prepared in an atmospheric environment using a method called spin coating. After the SiO<sub>2</sub>/Si substrate was cleaned, 30 μL of the aforementioned precursor solution was deposited on it. Afterward, the SiO<sub>2</sub>/Si substrate was put on a spin coater at 4000 rpm for 10 s, then 500 μL of diethyl ether was added dropwise and after 50 s of spin coating, in order to obtain the FA<sub>1-x</sub>Cs<sub>x</sub>PbI<sub>3</sub> samples. In order to obtain FA<sub>1-x</sub>Cs<sub>x</sub>PbI<sub>3</sub> thin films, the resulting films were annealed at 140 °C for 20 min.

### 2.3. Characterizations

The elemental distribution of the samples was investigated using energy-dispersive X-ray spectroscopy (EDX), while the morphology of the samples was observed using a scanning electron microscope (SEM, Quanta FEG 250). Steady-state photoluminescence (PL) spectra of the samples were taken using IK3301 spectroscopy and an excitation wavelength of 532 nm. X-ray diffraction experiments of the FA<sub>1-x</sub>Cs<sub>x</sub>PbI<sub>3</sub> thin film were carried out on a DX-2700 X-ray diffractometer. The Scientific Escalab 250 XPS spectrometer was used to conduct the X-ray photoelectron spectroscopy (XPS) on the samples. The ultraviolet–visible (UV–vis) light absorption spectra of the samples were obtained using a spectrometer model number UV-4100 (Hitachi). On a semiconductor integrated test system, the current–voltage (*I*-*V*) and current–time (*I*-*t*) curves of the devices as they were initially fabricated were recorded (Keithley 4200SCS, USA). The current and time of a periodically switched light source were tested by the Optical Chopper (New Focus 3502). The lamp used was Xenon Light (67005), a monochromatic light source at the wavelength of 790 nm, and the model was 918D-918D; additionally, an incandescent lamp with a wavelength in the visible light range with the model of MLC-150C was used.

### 2.4. Fabrication of FA<sub>1-x</sub>Cs<sub>x</sub>PbI<sub>3</sub> Thin-Film Photodetectors

Figure 1 provides a schematic representation of the fabrication process for an FA<sub>1-x</sub>Cs<sub>x</sub>PbI<sub>3</sub> thin-film photodetector. After the FA<sub>1-x</sub>Cs<sub>x</sub>PbI<sub>3</sub>-coated SiO<sub>2</sub>/Si substrate was secured with a mask (wound with a tungsten wire with a diameter of 10 μm), it was placed in an electron beam evaporator. To protect the perovskite film, an Au layer was deposited on top with a thickness of 80–100 nm. In the end, the SiO<sub>2</sub>/Si substrate was removed, and for the purpose of the subsequent electrical measurements, the two ends of the perovskite sample that were in contact with the Au electrodes were chosen.

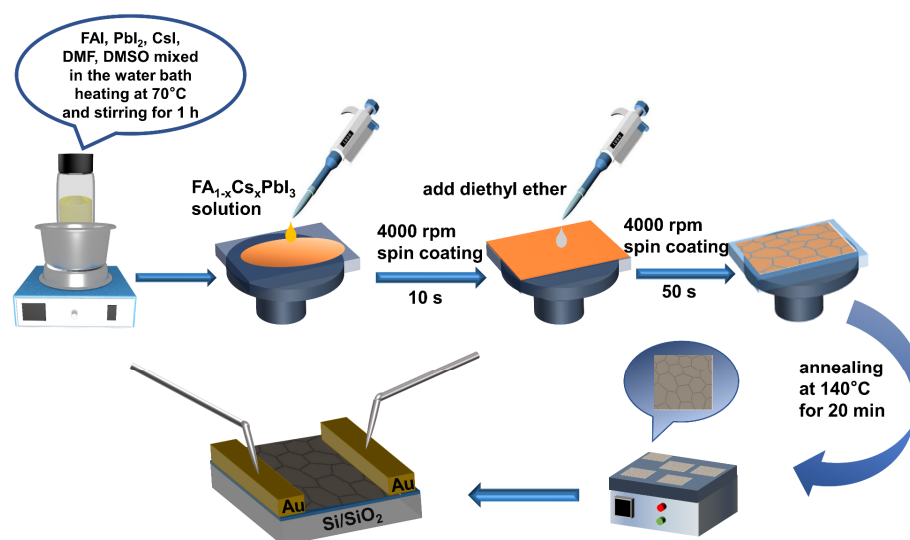


Figure 1. Flow chart of  $\text{FA}_{1-x}\text{Cs}_x\text{PbI}_3$  thin-film device preparation.

### 3. Results and Discussion

Figure 2a–c shows SEM images of as-prepared  $\text{FA}_{1-x}\text{Cs}_x\text{PbI}_3$  thin films with three different compositions, where  $x$  is equal to 0.10, 0.15, and 0.20, respectively. It is evident that a thin perovskite film can be manufactured with a large grain size when  $x$  is equal to 0.15, as this results in a film that is smooth, flat, and compact. Figure S1 is a statistical diagram and summary of the relevant SEM grain size data (Supporting Information, SI). A cross-sectional SEM image reveals that  $\text{FA}_{0.85}\text{Cs}_{0.15}\text{PbI}_3$  films have a uniformly thick epilayer and a clearly defined film-substrate interface (Figure 2d–f). The reason for the difference in film thickness can be ascribed to the varied concentration of precursor solution with the  $\text{Cs}^+$  doping. The corresponding effect of various  $\text{Cs}^+$  contents on the evolution of film morphology is depicted in Figure S2, which can be found in reference [19]. When  $x$  is equal to 0, 0.1, 0.2, 0.25, or 1, it is easy to discover that discontinuous films with obvious holes or defects will be formed. This result stands in striking contrast to the one that was obtained when  $x$  was equal to 0.15, in which a perovskite with a continuous film of relatively high quality was discovered. The  $\text{FA}_{0.85}\text{Cs}_{0.15}\text{PbI}_3$  thin film also has a smoother surface and more uniform element distribution, as seen in the SEM image of the  $\text{FA}_{1-x}\text{Cs}_x\text{PbI}_3$  thin film and the corresponding element mapping in Figure S3. This is indicative of higher crystallinity and fewer defects in the  $\text{FA}_{0.85}\text{Cs}_{0.15}\text{PbI}_3$  thin film. Therefore, the  $\text{Cs}^+$  contents play an important role in the evolution of the film's morphology [19].

The X-ray diffraction (XRD) patterns of  $\text{FA}_{1-x}\text{Cs}_x\text{PbI}_3$  samples with various Cs ratios ( $x = 0, 0.1, 0.15, \text{ and } 0.2$ ) are being researched to shed light on the effect that the concentration of  $\text{Cs}^+$  has on the perovskite structure. It is clear from Figure 3a that the  $\delta$ -FAPbI<sub>3</sub> phase exists at a diffraction angle of 11.8° when  $x = 0$  and 0.1 and that this phase is responsible for the bulk of the  $x = 0$  case. This is consistent with reports in the literature [12,31,32] and is the result of moisture-induced perovskite crystallization, which is unpredictable and randomly oriented. At  $x = 0.1$ , however, the  $\delta$ -FAPbI<sub>3</sub> phase begins to weaken, and by  $x = 0.15$ , it has almost completely disappeared. The results of which show that the formation of the  $\delta$ -FAPbI<sub>3</sub> phase can be promoted even at a Cs doping concentration of 15%. Moreover, the characteristic peaks of the (001), (110), (111), (002), (012), (211), (022), and (003) for  $\alpha$ -phase can be seen at diffraction angles of 14°, 19.8°, 24.2°, 28°, 31.5°, 40°, and 42°, respectively. The cubic structure is characterized by the diffraction peaks and their characteristic shapes. The XRD pattern of CsPbI<sub>3</sub> ( $x = 1$ ) is depicted in Figure 3b, and we can see that the characteristic diffraction peaks correspond very closely to those on the standard card (PDF#74-1970). Figure S5 displays the XRD patterns for the other individual  $\text{FA}_{1-x}\text{Cs}_x\text{PbI}_3$  thin films with the following values for  $x$ : 0, 0.1, 0.15, and 0.2. In the cases of  $x = 0$  and 0.1, the diffraction peaks at 12.7° corresponding to PbI<sub>2</sub> residue are observed

in Figure S5a,b. This is likely due to the FAI depletion and suppressed FAI intercalation into the underneath  $\text{PbI}_2$  [12]. In contrast, when the value of  $x$  was equal to 0.15, the  $\text{PbI}_2$  diffraction peak disappeared, illustrating the high-purity  $\text{FA}_{0.85}\text{Cs}_{0.15}\text{PbI}_3$  thin film.

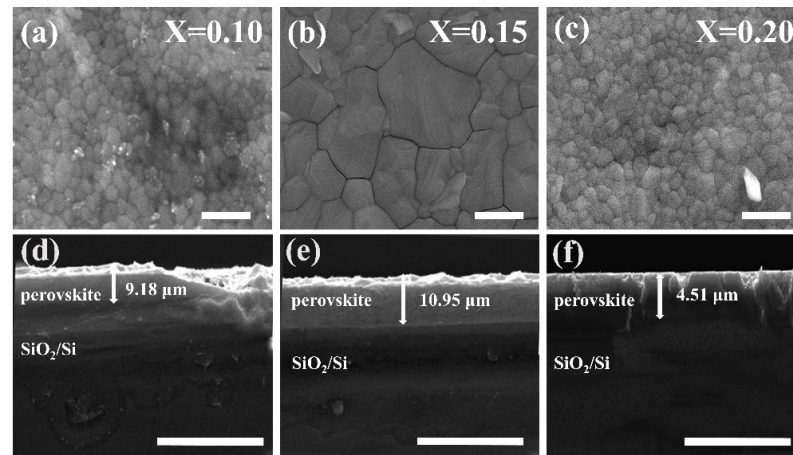


**Figure 2.** (a–c) SEM images of  $\text{FA}_{1-x}\text{Cs}_x\text{PbI}_3$  thin films with varying compositions ( $x = 0.10, 0.15,$  and  $0.20,$  respectively), scale bar,  $2 \mu\text{m}$ . (d–f) show the corresponding ( $x = 0.10, 0.15,$  and  $0.20,$  respectively) cross-section SEM image of the  $\text{FA}_{1-x}\text{Cs}_x\text{PbI}_3$  thin films; the thickness is  $9.18 \mu\text{m}, 10.95 \mu\text{m}, 4.51 \mu\text{m},$  respectively, scale bar,  $100 \mu\text{m}$ .

To further illustrate, Figure 3c displays the photoluminescence (PL) spectra of five  $\text{FA}_{1-x}\text{Cs}_x\text{PbI}_3$  samples with varying Cs ratios ( $x = 0, 1, 0.1, 0.15,$  and  $0.2$ ). At approximately  $750\text{--}830 \text{ nm}$ , it was discovered that each and every  $\text{FA}_{1-x}\text{Cs}_x\text{PbI}_3$  thin film exhibited a distinctive luminescence peak. According to the results of the normalized PL peaks, as the value of  $x$  increases from 0 to 0.1, 0.15 to 0.2, and 1, respectively, the peak of the  $\text{FA}_{1-x}\text{Cs}_x\text{PbI}_3$  thin film has a blue shift from 801 to 790, 789, 788, and 760 nm. The blue shift in the PL peak can be caused by the slightly increased band gap of the  $\text{FA}_{1-x}\text{Cs}_x\text{PbI}_3$  perovskites along with the increase in “ $x$ ” values. This phenomenon is consistent with the findings of an earlier study [28]. Moreover, in terms of peak intensity, wavelength position, and FWHM, when compared to thin films with other concentrations of  $\text{Cs}^+$  ( $x = 0, 1, 0.1,$  and  $0.2$ ), our results showed that our films had the best characteristics (Table S1). For  $x = 0, 1, 0.10, 0.15,$  and  $0.20,$  the calculated FWHM values are 44.15, 42.31, 42.58, 36.18, and 42.42 nm. When CsI is added, the FWHM decreases, which is consistent with larger crystallite size according to the Scherrer equation ( $D = K\lambda/\beta\cos\theta$ ), while an increase in FWHM above the value of  $x = 0.20$  is probably attributable to the formation of an impurity [28]. In accordance with the XRD results and in agreement with a previous study [28], the highest purity of the  $\alpha\text{-FAPbI}_3$  phase formed at  $x = 0.15$  is found in  $\text{FA}_{0.85}\text{Cs}_{0.15}\text{PbI}_3$ , indicating that when the Cs ratio is 15%, a suppressed non-radiative recombination induced by reduced traps and defects within the perovskite [12] supports the formation of the phase. The intensity decrease in PL can be ascribed to the presence of lattice defects and increased grain boundaries in the  $\text{FA}_{1-x}\text{Cs}_x\text{PbI}_3$  ( $x = 0, 1, 0.1,$  and  $0.2$ ) material with non-uniform film morphology. The presence of lattice defects and grain boundaries can increase the non-irradiation recombination of photogenerated charge carriers, giving rise to decreased PL intensity. In addition to this, the half width of the luminescence peak is at its narrowest when  $x$  is equal to 0.15, which indicates that the quality of the perovskite film is higher when this ratio is used. These results provide further confirmation of the important role that the  $\text{Cs}^+$  content plays in initiating the morphological evolution of the films.

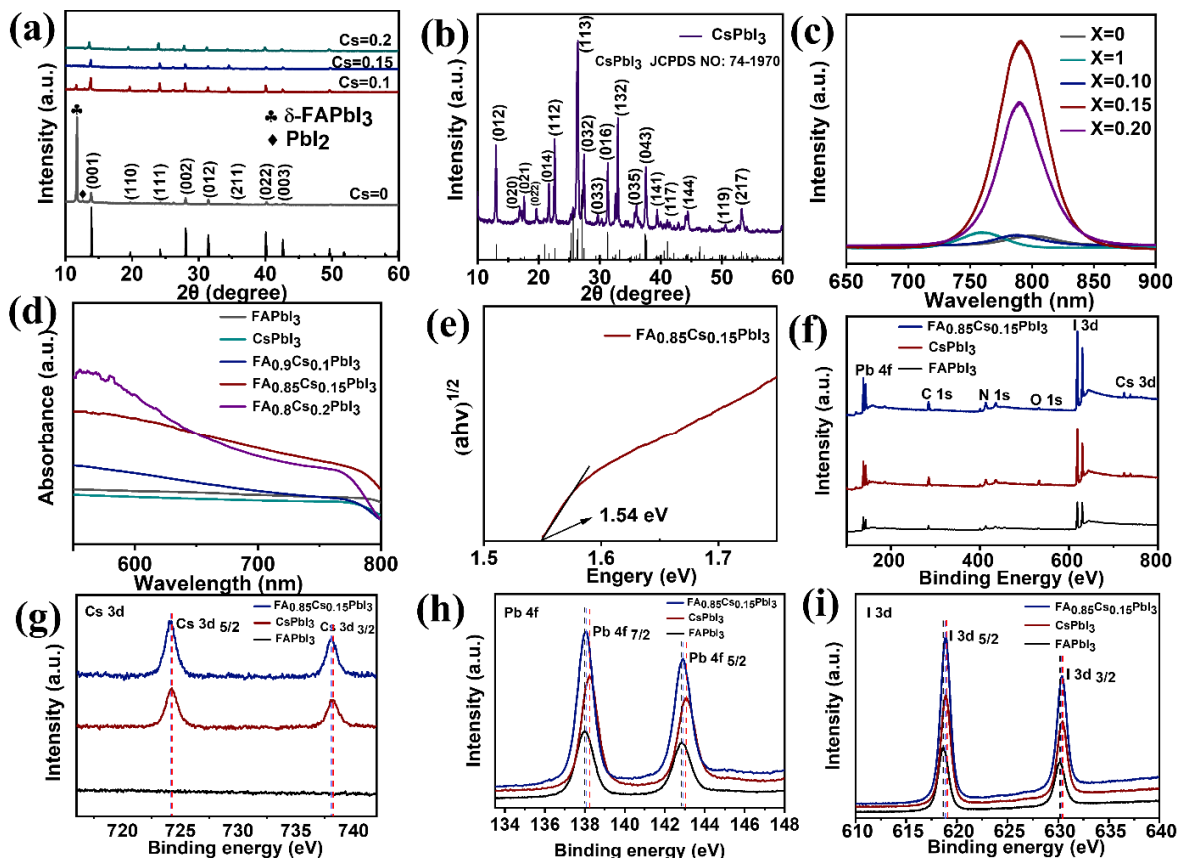


**Figure 3.** (a) XRD patterns of the FA<sub>1-x</sub>Cs<sub>x</sub>PbI<sub>3</sub> thin film ( $x = 0, 0.10, 0.15,$  and  $0.20,$  respectively); (b) XRD patterns of the CsPbI<sub>3</sub> thin film; (c) photoluminescence (PL) spectra of FA<sub>1-x</sub>Cs<sub>x</sub>PbI<sub>3</sub> thin film ( $x = 0, 1, 0.10, 0.15,$  and  $0.20,$  respectively); (d) the UV-vis absorbance spectra of FA<sub>1-x</sub>Cs<sub>x</sub>PbI<sub>3</sub> thin film ( $x = 0, 1, 0.10, 0.15,$  and  $0.20,$  respectively); (e) the relationship between  $(ahv)^{1/2}$  and photon energy of FA<sub>0.85</sub>Cs<sub>0.15</sub>PbI<sub>3</sub> thin film; (f) XPS spectra of FAPbI<sub>3</sub> (black), CsPbI<sub>3</sub> (red) and FA<sub>0.85</sub>Cs<sub>0.15</sub>PbI<sub>3</sub> (blue) thin film; (g–i) the corresponding Cs 3d, Pb 4f and I 3d spectra, respectively.

Figure 3d shows the corresponding ultraviolet–visible (UV-vis) absorbance spectra of the FA<sub>1-x</sub>Cs<sub>x</sub>PbI<sub>3</sub> thin films; we can see the FA<sub>0.85</sub>Cs<sub>0.15</sub>PbI<sub>3</sub> thin film exhibits the strongest absorbance. The UV-vis spectra of FA<sub>1-x</sub>Cs<sub>x</sub>PbI<sub>3</sub> thin films ( $x = 0, 0.1, 0.2,$  and  $1$ ) are blue-shifted compared to that of FA<sub>0.85</sub>Cs<sub>0.15</sub>PbI<sub>3</sub> thin film. The combined characterizations of PL, XRD, and SEM suggest that FA<sub>0.85</sub>Cs<sub>0.15</sub>PbI<sub>3</sub> thin film has large grain sizes, low defect density, and a small band gap. Compared to FA<sub>0.85</sub>Cs<sub>0.15</sub>PbI<sub>3</sub> thin film, other FA<sub>1-x</sub>Cs<sub>x</sub>PbI<sub>3</sub> ( $x = 0, 0.1, 0.2,$  and  $1$ ) thin films showed blue shift due to their larger band gaps. Then the band gap of FA<sub>0.85</sub>Cs<sub>0.15</sub>PbI<sub>3</sub> thin film, as shown in Figure 3e, was calculated via the transformed Kubelka–Munk formula [33]:

$$\alpha(hv) = A(hv - E_g)^{1/2} \tag{2}$$

where  $\alpha$  signifies the absorption coefficient,  $hv$  is the incident photon energy,  $A$  represents the constant depending on transition probability, and  $E_g$  is the optical bandgap. Accordingly, the band gap of 1.54 eV for FA<sub>0.85</sub>Cs<sub>0.15</sub>PbI<sub>3</sub> thin film is obtained, which is similar to the previous study [19].

In order to investigate the effect that doping with Cs had on the chemical composition of perovskite films, X-ray photoelectron spectroscopy (XPS) was utilized. For FAPbI<sub>3</sub>, CsPbI<sub>3</sub>, and FA<sub>0.85</sub>Cs<sub>0.15</sub>PbI<sub>3</sub>, the core level peaks assigned to C, N, O, Cs (except for FAPbI<sub>3</sub>), Pb, and I are shown in Figure 3f. Several sets of results for various Cs<sup>+</sup> concentrations are shown in Figure S4. Figure 3g is an XPS spectrum of the Cd 3d<sub>5/2</sub> and Cd 3d<sub>3/2</sub> peaks, showing that the peaks in FA<sub>0.85</sub>Cs<sub>0.15</sub>PbI<sub>3</sub> are at 724.1 eV and 738.1 eV, while

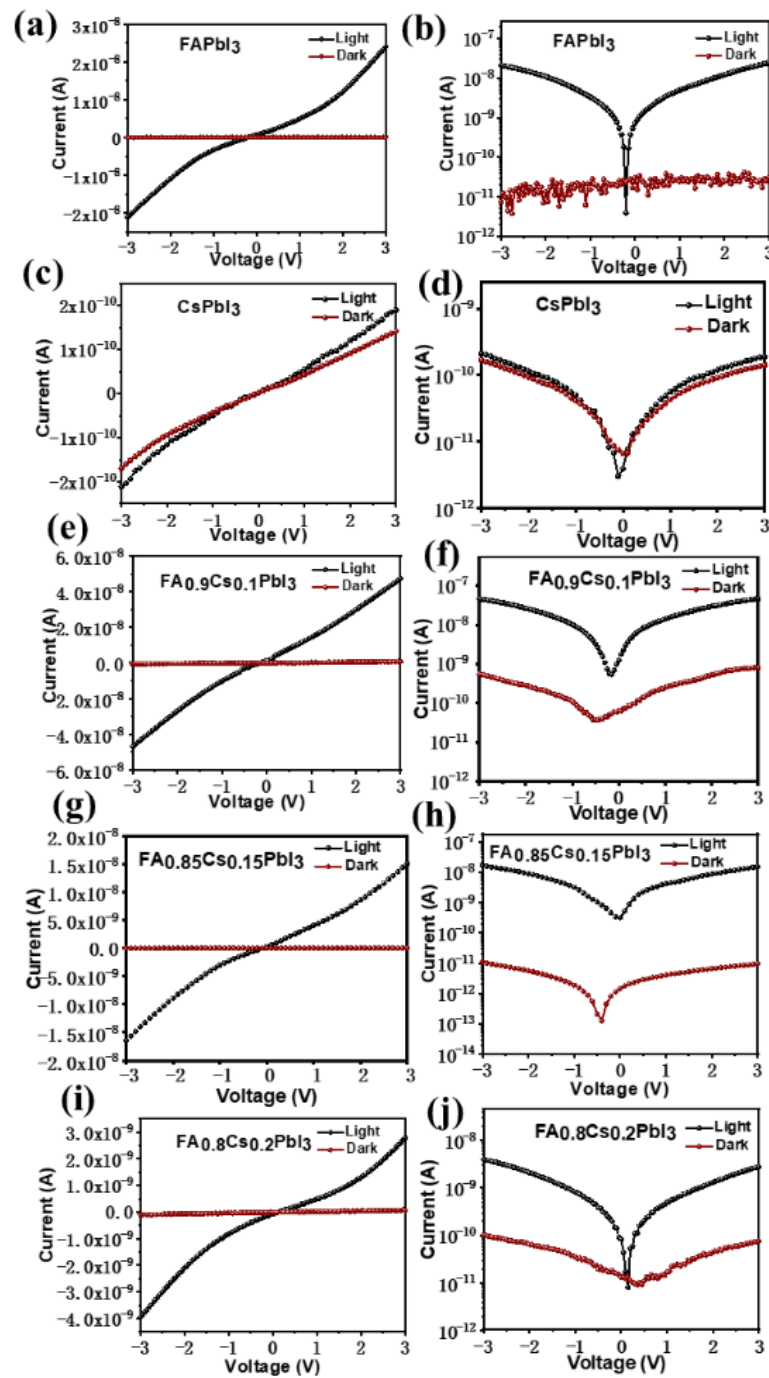
the peaks in CsPbI<sub>3</sub> are at 724.2 eV and 738.2 eV. These results indicate that there is no Cs signal characteristic in FAPbI<sub>3</sub> thin film. Since the bond energy between Cs<sup>+</sup> and [PbI<sub>6</sub>]<sup>4-</sup> is stronger than that between FA<sup>+</sup> and [PbI<sub>6</sub>] [34], both Cd 3d<sub>5/2</sub> and Cd 3d<sub>3/2</sub> of CsPbI<sub>3</sub> move 0.1 eV towards higher binding energy compared to FA<sub>0.85</sub>Cs<sub>0.15</sub>PbI<sub>3</sub>.

Figure 3h displays the Pb 4f spectrum of FAPbI<sub>3</sub>, which has two peaks at 138.0 eV and 142.8 eV, which correspond to Pb 4f<sub>7/2</sub> and Pb 4f<sub>5/2</sub>, respectively. When comparing FA<sub>0.85</sub>Cs<sub>0.15</sub>PbI<sub>3</sub> to FAPbI<sub>3</sub>, the binding energies of both Pb 4f<sub>5/2</sub> and Pb 4f<sub>7/2</sub> move up by 0.1 eV. The shift of Pb 4f peaks towards higher binding energy is indicative of an increase in the cationic charge of Pb ions, which is responsible for the change in the chemical bonding nature between Pb and I [35]. This change in bonding nature is responsible for the fact that the Pb 4f peaks shifted towards higher binding energy. It is clear that the bond energy between Cs<sup>+</sup> and [PbI<sub>6</sub>]<sup>4-</sup> is stronger than that between FA<sup>+</sup> and [PbI<sub>6</sub>]<sup>4-</sup> because the binding energies of Pb 4f<sub>7/2</sub> and Pb 4f<sub>5/2</sub> of CsPbI<sub>3</sub> are higher than those of FA<sub>0.85</sub>Cs<sub>0.15</sub>PbI<sub>3</sub>, respectively (by 0.1 eV and 0.2 eV, respectively). In addition, there was some variation in the I elements representing the formamidine building blocks (Figure 3i). Table 1 presents the corresponding values for the binding energies. These findings provide additional evidence that Cs was able to be successfully incorporated into the FAPbI<sub>3</sub> perovskite lattice to produce the FA<sub>0.85</sub>Cs<sub>0.15</sub>PbI<sub>3</sub> perovskite.

**Table 1.** The XPS data comparison of FAPbI<sub>3</sub>, CsPbI<sub>3</sub>, and FA<sub>0.85</sub>Cs<sub>0.15</sub>PbI<sub>3</sub> for Cs 3d, Pb 4f, and I 3d core levels.

Binding Energy (eV)	FAPbI <sub>3</sub>	CsPbI <sub>3</sub>	FA <sub>0.85</sub> Cs <sub>0.15</sub> PbI <sub>3</sub>
I 3d <sub>3/2</sub>	630.2	630.5	630.4
I 3d <sub>5/2</sub>	618.7	619.0	618.9
Pb 4f <sub>5/2</sub>	142.8	143.1	142.9
Pb 4f <sub>7/2</sub>	138.0	138.2	138.1
Cs 3d <sub>3/2</sub>	–	738.2	738.1
Cs 3d <sub>5/2</sub>	–	724.2	724.1

We fabricated FA<sub>1-x</sub>Cs<sub>x</sub>PbI<sub>3</sub>-based optoelectronic devices by depositing an Au electrode on the surface of FA<sub>1-x</sub>Cs<sub>x</sub>PbI<sub>3</sub> thin film. This allowed us to study the optoelectronic properties of the FA<sub>1-x</sub>Cs<sub>x</sub>PbI<sub>3</sub> thin film. Figure 4 depicts the current–voltage (*I*-*V*) characteristics of FA<sub>1-x</sub>Cs<sub>x</sub>PbI<sub>3</sub> thin-film photodetectors doped with various concentrations of Cs<sup>+</sup> at room temperature and atmospheric pressure and under illumination from an incandescent lamp with a power density of 21.57 mW/cm<sup>2</sup> in the dark. The on/off ratios of the photodetectors of FAPbI<sub>3</sub>, CsPbI<sub>3</sub>, FA<sub>0.9</sub>Cs<sub>0.1</sub>PbI<sub>3</sub>, FA<sub>0.85</sub>Cs<sub>0.15</sub>PbI<sub>3</sub>, and FA<sub>0.8</sub>Cs<sub>0.2</sub>PbI<sub>3</sub> samples were calculated as 1.32, 0.77 × 10<sup>3</sup>, 0.66 × 10<sup>2</sup>, 1.58 × 10<sup>3</sup>, and 0.43 × 10<sup>2</sup>, respectively. The variation in current that occurs when the bias voltage changes from −3 V to 3 V is shown, and all of the Cs<sup>+</sup> concentration results for doping indicate that the photocurrent is significantly higher than the dark current. It is likely that the surface state (such as surface defects and vacancies) at the FAPbI<sub>3</sub>/Au interface [36] is responsible for the asymmetrical behavior of the *I*-*V* curves observed for pure FAPbI<sub>3</sub>, as shown in Figure 4a,b. However, when doped with varying concentrations of Cs<sup>+</sup> (*x* = 1, 0.1, 0.15, and 0.2, respectively), as shown in Figure 4c-j, there is an ohmic contact formed between the FA<sub>1-x</sub>Cs<sub>x</sub>PbI<sub>3</sub> thin film and the Au electrode because the *I*-*V* curves are almost symmetric. Under a bias voltage of 3 V, the photocurrent in the FA<sub>0.85</sub>Cs<sub>0.15</sub>PbI<sub>3</sub> thin-film photodetector is 1.51 × 10<sup>-8</sup> A, the dark current is 9.54 × 10<sup>-12</sup> A, and the ratio of photocurrent to dark current (*I*<sub>light</sub>/*I*<sub>dark</sub>) is 1.58 × 10<sup>3</sup>, as shown in Figure 4g,h. As a result of the fact that the ratio of photocurrent to dark current in the other Cs<sup>+</sup> doping concentrations (*x* = 0, 0.1, 0.2, 1) is relatively smaller in comparison to the FA<sub>0.85</sub>Cs<sub>0.15</sub>PbI<sub>3</sub> thin-film device, it is not conducive to the preparation and research of photodetectors. As a result, the photoconductive characteristics of the FA<sub>0.85</sub>Cs<sub>0.15</sub>PbI<sub>3</sub> thin-film device is studied in the majority of this research.



**Figure 4.** (a,c,e,g,i) *I-V* curve of the FA<sub>1-x</sub>Cs<sub>x</sub>PbI<sub>3</sub> thin-film device in light (black) and dark (red) conditions, respectively; (b,d,f,h,j) correspond to the (a,c,e,g,i) after logarithmic processing, respectively.

We measured the spectral response curves of the FA<sub>0.85</sub>Cs<sub>0.15</sub>PbI<sub>3</sub> thin-film device in the range of 530–830 nm in order to gain more insights into the optimal spectra of the FA<sub>0.85</sub>Cs<sub>0.15</sub>PbI<sub>3</sub> thin film. These curves are shown in Figure 5b, and they are elucidated in more detail below. The spectral response of the FA<sub>0.85</sub>Cs<sub>0.15</sub>PbI<sub>3</sub> thin film exhibits a wide photoresponse range, which extends from 560 to 790 nm. However, the photoresponse decreases dramatically at approximately 790 nm. The device’s best wavelength selectivity is demonstrated by the fact that its largest photoresponse is at 790 nm. As a result, we intend to investigate the photoelectric characteristics of a thin-film device made from FA<sub>0.85</sub>Cs<sub>0.15</sub>PbI<sub>3</sub> while exposed to 790 nm light.

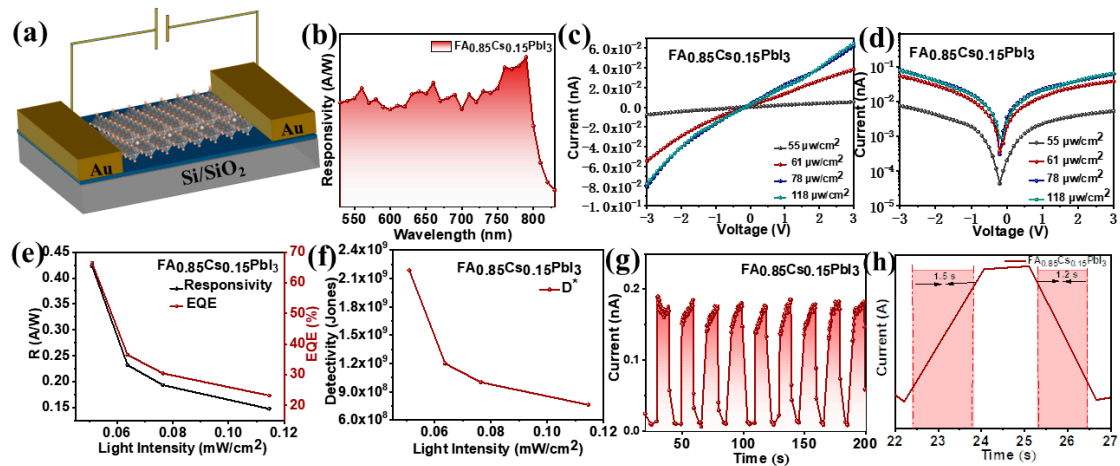


**Figure 5.** (a) Schematic illustration of the  $FA_{1-x}Cs_xPbI_3$  photodetector; (b) spectral responsivity of the  $FA_{0.85}Cs_{0.15}PbI_3$  thin-film photodetector at 3 V bias; (c)  $I$ - $V$  curves of the  $FA_{0.85}Cs_{0.15}PbI_3$  thin-film device at different light power density; (d)  $I$ - $V$  curves of (c) after logarithmic processing; (e) diagrams of responsivity and optical power density; (f) relationship between detectivity and optical power density; (g) the  $FA_{0.85}Cs_{0.15}PbI_3$  thin-film device relationship between the current and time of a periodically switched light source under 790 nm light illumination at a bias of 3 V; (h) voltage rise and decay edge of pulse response.

The  $I$ - $V$  curves at varying light intensities for the prepared  $FA_{0.85}Cs_{0.15}PbI_3$  thin-film photodetector are shown in Figure 5c. From the  $I$ - $V$  curves, one can see that the photocurrent increases dramatically with an increase in light intensity, suggesting that the number of photogenerated carriers is related to the absorbed photon fluxes [37]. As shown in Figure 5d, for the  $I$ - $V$  curve of (c) after logarithmic processing, the logarithmic  $I$ - $V$  plot displays near symmetry at voltage biases of ( $-3$  V– $3$  V), indicating that the ohmic contacts between the  $FA_{0.85}Cs_{0.15}PbI_3$  thin-film surfaces and the deposited Au electrodes are strong.

In order to conduct a more in-depth analysis of the performance of the  $FA_{0.85}Cs_{0.15}PbI_3$  thin-film device, important parameters such as spectral responsivity ( $R$ ), external quantum efficiency ( $EQE$ ), and detection rate ( $D^*$ ) were computed by making use of the following equations [38–40]:

$$R_\lambda = \frac{I_p - I_d}{P_\lambda A} \quad (3)$$

$$EQE = R_\lambda \left( \frac{hc}{q\lambda} \right) \frac{1}{\eta} \quad (4)$$

$$D^* = R_\lambda \sqrt{\frac{A}{2qI_d}} \quad (5)$$

where  $I_p$  is the photocurrent,  $I_d$  is the dark current,  $P$  is the light power density,  $A$  is the detector’s valid area,  $h$  is the Planck constant,  $c$  is the speed of light in a vacuum,  $q$  is the charge of an electron,  $\lambda$  is the wavelength of the incident light, and  $EQE$  is the quantum efficiency. In our work, the distance between the source light and the photodetector is 1.8 cm, and the effective area of illumination is  $3.634 \times 10^{-5} \text{ cm}^2$ . According to the information presented above, it was determined that the  $R$ ,  $EQE$ , and  $D^*$  values of the devices when exposed to light with a wavelength of 790 nm are, respectively, 0.42 A/W, 66.5%, and  $2.2 \times 10^9$  Jones. As shown in Figure 5e,f, the decrease in response can be attributed to the deterioration of the  $FA_{0.85}Cs_{0.15}PbI_3$  thin film, which was influenced by the light and the air around it. In addition, from the curves of  $R$ ,  $EQE$ , and  $D^*$  corresponding to the  $FA_{0.85}Cs_{0.15}PbI_3$  thin-film device with light intensity, we can see that  $R$ ,  $EQE$ , and  $D^*$  decrease with the increase in light intensity, indicating that the recombination loss in the device cannot be ignored.

In Figure 5g, the findings demonstrate that chopper illumination can efficiently and reproducibly alter the FA<sub>0.85</sub>CS<sub>0.15</sub>PbI<sub>3</sub> thin-film device’s low and high current conduction states. In Figure 5h, we see a single cycle of FA<sub>0.85</sub>CS<sub>0.15</sub>PbI<sub>3</sub> thin film’s response, which reflects the response time, are, respectively, 1.5 and 1.2 s, which is defined as the time it takes for the value to rise from 10% to 90% of its maximum and fall back down to 10% of its maximum value. This is the rise time and decay time, respectively [41]. The FA<sub>0.85</sub>CS<sub>0.15</sub>PbI<sub>3</sub> thin film deterioration may be related to its slow degradation rate. This indicates that the performance of FA<sub>0.85</sub>CS<sub>0.15</sub>PbI<sub>3</sub> thin film photodetector is still inadequate. As can be seen in Table 2, we compared the performance of the reported results. In addition, Figure 6 exhibits the *I-V* curves of the as-fabricated device after being stored in the air for five days (red curve). It was found that the photocurrent was 2.17 nA under 3 V bias; the device dropped to 14.3% of its initial value after being stored in the air for 5 days (black curve). In summary, the performance of formamidinium-based perovskites is impacted by their level of stability. Next, we discuss the factors that affect stability.

**Table 2.** Performance comparison of different photodetectors.

Device Structure	Method	Wavelength (nm)	$I_{light}/I_{dark}$	$R_{\lambda}$ (A W <sup>-1</sup> )	EQE (%)	D* (Jones)	Rise/Decay (ms)	Ref
Au/(BA) <sub>2</sub> FAPb <sub>2</sub> I <sub>7</sub> /	-	405	-	0.95	-	-	62/57	[42]
ITO/MA <sub>1-x</sub> FA <sub>x</sub> (Br <sub>0.65</sub> C <sub>10.35</sub> ) <sub>3</sub> thin film/Au	A-site compositional	450	$5.72 \times 10^5$	0.28	77.4	$5.08 \times 10^{12}$	585/531	[43]
ITO/SnO <sub>2</sub> /FAPbI <sub>3</sub> /Spiro-OMeTAD/Ag	Additive engineering	700	-	0.48	95	$2 \times 10^{11}$	0.00394/0.00476	[44]
FTO/CS <sub>0.05</sub> MA <sub>0.16</sub> FA <sub>0.79</sub> Pb(I <sub>0.9</sub> Br <sub>0.1</sub> ) <sub>3</sub> /Spiro/Au	-	-	$7.3 \times 10^5$	0.52	-	$8.8 \times 10^{12}$	0.019/0.021	[45]
PET/ITO/SnO <sub>2</sub> /Active layer/CuI/Au Active layer: MBI, MBIB, MBIC films	chemical-vapor-deposited	382	-	0.30(MBI) 0.63(MBIB) 0.92(MBIC)	-	$0.9 \times 10^{13}$ $2 \times 10^{13}$ $2.9 \times 10^{13}$	-	[46]
Pt NP@TiO <sub>2</sub> /Ga <sub>2</sub> N NRs	-	382	-	44.6	$8.65 \times 10^3$	$1.57 \times 10^{14}$	180/200	[47]
Au NPs@ZnO NWs	hydrothermal	325	-	0.000485	-	$27.49 \times 10^{10}$	-	[48]
SiO <sub>2</sub> /FA <sub>0.85</sub> CS <sub>0.15</sub> PbI <sub>3</sub> thin film/Au	solution	790	$1.58 \times 10^3$	0.42	66.5	$2.2 \times 10^9$	1500/1200	This work

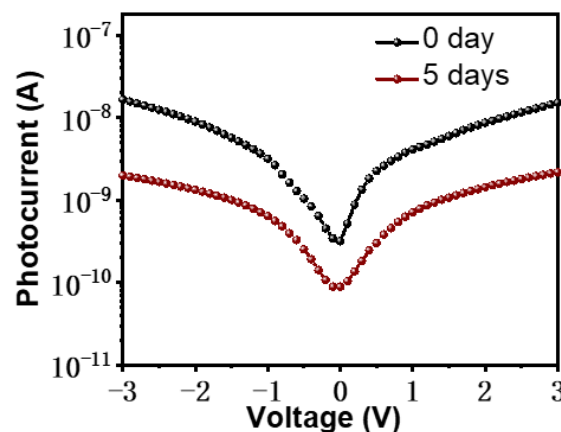


**Figure 6.** *I-V* curve of the initial photocurrent (black curve) of FA<sub>0.85</sub>CS<sub>0.15</sub>PbI<sub>3</sub> thin film and after five days (red curve).

The stability of a perovskite based on formamidinium can be broken down into two categories: intrinsic properties and environmental influences, considering the influence of ambient air oxygen and moisture levels. For example, in the mapping characterization of FA<sub>0.85</sub>CS<sub>0.15</sub>PbI<sub>3</sub> thin film, we can observe the rich oxygen element part from the oxygen component that is possible from the oxygen in the air that has been adsorbed on its surface, which is also the reason why its possible degradation is a possibility. It has been reported that oxygen molecules that are adsorbed on perovskite films can obtain photogenerated

electrons to form superoxide ions when the film is illuminated. These superoxide ions are then easily dehydrogenated with organic cations in perovskite, which leads to the decomposition of perovskite crystals (photo-oxygen-induced decomposition). It has been discovered that the incorporation of moderate  $\text{Cs}^+$  ions into  $\text{MAPbI}_3$  or formamidinium-based perovskite acts as a powerful stabilizer, preventing the decomposition of the perovskite in the presence of oxygen and light [49]. It has also been shown that perovskite crystalline materials such as  $\text{MAPbI}_3$  tend to decompose to  $\text{PbI}_2$  when exposed to moisture because of the bonding interactions between  $\text{MA}^+$  and  $\text{H}_2\text{O}$  molecules. Niu et al. [50] proposed that perovskite degradation starts with the deprotonation of methylammonium cations by water to produce methylamine, hydrogen iodide, and lead iodide, which breaks down the bonding. On the other hand, the same bond is present between  $\text{FAPbI}_3$  molecules and  $\text{H}_2\text{O}$  molecules. To prevent moisture from penetrating and increase device stability, Chen et al. [51] introduced trace amounts of hydrophobic molecules from outside the perovskite layers. In addition, light and electric fields, etc., can also have an effect on its performance. For example, Liu et al. [52] prepared an innovative resistive memory based on  $\text{CsPbBr}_3$  QDs:GO hybrid film by controlling the light and electric fields of the device, which exhibited good performance. Meng et al. [48] reported outstanding SPUVPD performances of the Pt NP@ $\text{TiO}_2$ /GaN NRs hybrid heterojunction, which was due to the abundant light absorption and better charge collection (hot electrons) by the enhanced LSPR effect and the adequate interfacial charge separation of photogenerated e/h pairs by its enhanced built-in field and the effective charge transport via the appropriate energy band alignment. As a result, the effective coupling effect of the LSPR effect of Pt NP with  $\text{TiO}_2$ /GaN NRs heterojunction significantly enhances the optoelectrical properties.

A number of intrinsic factors, such as ion migration [53,54], phase instability [55,56], metal-perovskite reactions [57], residual strain [57], photoinduced strain [58], etc., contribute to the instability of perovskite devices [59]. Once ion migration has taken place in perovskite materials, the loss of perovskite ions causes the perovskite lattice to collapse, which results in changes to the composition and morphology of perovskite films. Perovskite materials are doomed to destruction if a process known as dynamic ion migration is allowed to take place [57]. Xia et al. [60] demonstrated strong photoinduced polarization strain in triple-cation mixed-halide perovskite CsFAMA by examining the concurrent evolution of ionic distribution and spontaneous polarization of CsFAMA under light illumination using dynamic-strain-based scanning probe microscopy. Strong linear piezoelectricity arising from photo-enhanced polarization was observed, while ionic migration was found to be not significantly increased by lightening. Their research proved that ionic migration, polarization, and photocurrent hysteresis are directly correlated at the nanoscale.

It has been found that the phenomenon of ion migration in the  $\text{MAPbI}_3$  thin film can make the process of photo-oxygen-induced decomposition inside the perovskite even more severe. This is the case due to the fact that the movement of iodide ions, while they are subject to an electric field, can result in the formation of iodine vacancies (defects), and the accumulation of iodine vacancies can increase the generation rate of superoxide ions and speed up the process of photo-oxygen-induced decomposition of perovskites [49]. Additionally, Li et al. [58] observed that the photoinduced strain-promoted variations in mechanical properties were caused by the reversible migration of  $\text{MA}^+$  cations. However,  $\text{FAPbI}_3$  is prone to phase transition at room temperature ( $\alpha \rightarrow \delta$  phase transition), and pure  $\alpha$ -phase  $\text{FAPbI}_3$  perovskite generally requires high annealing temperature, both of which degrade the stability of the device. It has been shown that Au atoms/ions can diffuse through organic hole transport layers into the perovskite layer and react with the perovskite [61], and such Au-perovskite reactions can be promoted by continuous light illumination and high thermal stress. A systematic investigation into the mechanism of Au electrode degradation due to reaction with iodine-based perovskites was reported by Tarasov et al. [62]. At room temperature, they discovered that the reactive MAI-nI<sub>2</sub> tends to oxidize the Au electrodes, leading to the formation of a new  $(\text{MA})_2\text{Au}_2\text{I}_6$  phase at the perovskite/Au interface. This demonstrates that the metal-perovskite reaction has

an effect on the stability of the device's performance. Because of their polycrystalline structure, organometallic perovskites are also subject to the detrimental effects of lattice strain on the residual strain. It has been shown that during film formation in perovskite, residual strain can be generated in the lattice via thermal annealing [63]. Specifically, lattice strain within the thin film would induce chemical degradation of the perovskite after it has been cooled down from a thermal annealing state because the substrate would prevent the perovskite from shrinking. It is also possible for the hybrid perovskites to experience material inhomogeneity as a result of component separation [64,65] and/or thermal stress, which may result from chemical mismatches between the components and/or from non-equilibrium growth conditions during film fabrication [66]. Furthermore, phase separation is thought to be a serious material inhomogeneity that deviates from the initially expected material properties and reduces device performance (efficiency and operational stability) [67,68]. There is a correlation between emerging residual strain and local lattice mismatch in thin films, which indicates a moderate level of material inhomogeneity. The crystal microstructure of the perovskite thin film can be distorted by this residual strain, which can have an effect on the film's properties [66,69–73].

#### 4. Conclusions

In conclusion,  $\text{FA}_{1-x}\text{Cs}_x\text{PbI}_3$  thin films were successfully synthesized in the atmospheric environment using the simple solution method. It was demonstrated, on the basis of a number of characterization results, that the  $\text{Cs}^+$  doping concentration is relatively ideal when set at 15%. Furthermore,  $\text{FA}_{0.85}\text{Cs}_{0.15}\text{PbI}_3$  thin film was prepared into an optoelectronic device for the purpose of research, and it was discovered that the photoelectric characteristics are affected by degradation factors; consequently, the possible degradation factors were discussed. Our results highlight the significance of controlling doped Cs concentrations and gaining insight into their potential degradation factors, which serve as a benchmark for the systematic optimization of FA-based perovskite devices, paving the way for their use in photovoltaics and other fields.

**Supplementary Materials:** The following supporting information can be downloaded at: <https://www.mdpi.com/article/10.3390/photonics10030312/s1>, Figure S1: (a–e) SEM images of  $\text{FA}_{1-x}\text{Cs}_x\text{PbI}_3$  thin films with different  $\text{Cs}^+$  contents ( $x = 0, 0.10, 0.15, 0.20$  and  $1$ , respectively). (f) Statistical diagram of the grain sizes of the  $\text{FA}_{1-x}\text{Cs}_x\text{PbI}_3$  thin films; Figure S2: (a–f) SEM images of  $\text{FA}_{1-x}\text{Cs}_x\text{PbI}_3$  thin films with different  $\text{Cs}^+$  contents ( $x = 0, 0.10, 0.15, 0.20, 0.25$ , and  $1.0$ , respectively); Figure S3: EDX elemental mapping of  $\text{FA}_{0.85}\text{Cs}_{0.15}\text{PbI}_3$  thin film; Figure S4: Survey XPS spectra of (a)  $\text{FA}_{0.9}\text{Cs}_{0.1}\text{PbI}_3$  and (b)  $\text{FA}_{0.8}\text{Cs}_{0.2}\text{PbI}_3$ , respectively; Figure S5: (a–d) XRD patterns of  $\text{FAPbI}_3$ ,  $\text{FA}_{0.9}\text{Cs}_{0.1}\text{PbI}_3$ ,  $\text{FA}_{0.85}\text{Cs}_{0.15}\text{PbI}_3$  and  $\text{FA}_{0.8}\text{Cs}_{0.2}\text{PbI}_3$  thin films, respectively; Table S1: The PL data of  $\text{FA}_{1-x}\text{Cs}_x\text{PbI}_3$  thin films ( $x = 0, 1, 0.1, 0.15$  and  $0.2$ , respectively) with peak intensity, wavelength position, and FWHM.

**Author Contributions:** Conceptualization, F.W. and X.Z.; methodology, F.W. and S.D.; software, F.W. and S.D.; validation, F.W., J.M. and Z.L.; formal analysis, F.W., S.D. and X.Z.; investigation, F.W.; resources, W.Z. and H.-E.W.; data curation, F.W. and S.D.; writing—original draft preparation, F.W., S.D. and X.Z.; writing—review and editing, P.M., J.M., Z.L., T.Z. and H.-E.W.; visualization, F.W.; supervision, H.-E.W.; project administration, H.-E.W.; funding acquisition, H.-E.W. All authors have read and agreed to the published version of the manuscript.

**Funding:** This research was funded by the National Science Foundation of Yunnan Province (Grant No. 202201AT070041) and Spring City Plan: The High-level Talent Promotion and Training Project of Kunming (2022SCP005).

**Institutional Review Board Statement:** Not applicable.

**Informed Consent Statement:** Not applicable.

**Data Availability Statement:** Data can be obtained from the authors upon reasonable request.

**Conflicts of Interest:** The authors declare no conflict of interest.

## References

1. Zheng, Z.; Wang, S.; Hu, Y.; Rong, Y.; Mei, A.; Han, H. Development of formamidinium lead iodide-based perovskite solar cells: Efficiency and stability. *Chem. Sci.* **2022**, *13*, 2167–2183. [[CrossRef](#)] [[PubMed](#)]
2. Murugan, P.; Hu, T.; Hu, X.; Chen, Y. Advancements in organic small molecule hole-transporting materials for perovskite solar cells: Past and future. *J. Mater. Chem. A* **2022**, *10*, 5044–5081. [[CrossRef](#)]
3. Murugan, P.; Hu, T.; Hu, X.; Chen, Y. Current Development toward Commercialization of Metal-Halide Perovskite Photovoltaics. *Adv. Opt. Mater.* **2021**, *9*, 2100390. [[CrossRef](#)]
4. Zhang, X.; Han, D.; Wang, C.; Muhammad, I.; Zhang, F.; Shmshad, A.; Xue, X.; Ji, W.; Chang, S.; Zhong, H. Highly Efficient Light Emitting Diodes Based on In Situ Fabricated FAPbI<sub>3</sub> Nanocrystals: Solvent Effects of On-Chip Crystallization. *Adv. Opt. Mater.* **2019**, *7*, 1900774. [[CrossRef](#)]
5. Yang, Y.; Xu, S.; Ni, Z.; Van Brackle, C.H.; Zhao, L.; Xiao, X.; Dai, X.; Huang, J. Highly Efficient Pure-Blue Light-Emitting Diodes Based on Rubidium and Chlorine Alloyed Metal Halide Perovskite. *Adv. Mater.* **2021**, *33*, e2100783. [[CrossRef](#)] [[PubMed](#)]
6. Fu, Y.; Zhu, H.; Schrader, A.W.; Liang, D.; Ding, Q.; Joshi, P.; Hwang, L.; Zhu, X.Y.; Jin, S. Nanowire Lasers of Formamidinium Lead Halide Perovskites and Their Stabilized Alloys with Improved Stability. *Nano Lett.* **2016**, *16*, 1000–1008. [[CrossRef](#)] [[PubMed](#)]
7. Wang, Y.; Song, L.; Chen, Y.; Huang, W. Emerging New-Generation Photodetectors Based on Low-Dimensional Halide Perovskites. *ACS Photonics* **2019**, *7*, 10–28. [[CrossRef](#)]
8. Mei, F.; Sun, D.; Mei, S.; Feng, J.; Zhou, Y.; Xu, J.; Xiao, X. Recent progress in perovskite-based photodetectors: The design of materials and structures. *Adv. Phys. X* **2019**, *4*, 1592709. [[CrossRef](#)]
9. Arya, S.; Mahajan, P.; Gupta, R.; Srivastava, R.; Kumar Tailor, N.; Satapathi, S.; Sumathi, R.R.; Datt, R.; Gupta, V. A comprehensive review on synthesis and applications of single crystal perovskite halides. *Prog. Solid State Chem.* **2020**, *60*, 100286. [[CrossRef](#)]
10. Yang, S.; Xu, Y.; Hao, Z.; Qin, S.; Zhang, R.; Han, Y.; Du, L.; Zhu, Z.; Du, A.; Chen, X.; et al. Recent Advances in High-Efficiency Perovskite for Medical Sensors. *Acta Phys. Chim. Sin.* **2022**, *39*, 2211025. [[CrossRef](#)]
11. Zhang, G.; Xu, Y.; Yang, S.; Ren, S.; Jiao, Y.; Wang, Y.; Ma, X.; Li, H.; Hao, W.; He, C. Robust mica perovskite photoelectric resistive switching memory. *Nano Energy* **2023**, *106*, 108074. [[CrossRef](#)]
12. Xu, X.; Ma, C.; Xie, Y.-M.; Cheng, Y.; Tian, Y.; Li, M.; Ma, Y.; Lee, C.-S.; Tsang, S.-W. Air-processed mixed-cation Cs<sub>0.15</sub>FA<sub>0.85</sub>PbI<sub>3</sub> planar perovskite solar cells derived from a PbI<sub>2</sub>-CsI-FAI intermediate complex. *J. Mater. Chem. A* **2018**, *6*, 7731–7740. [[CrossRef](#)]
13. Leijtens, T.; Bush, K.; Cheacharoen, R.; Beal, R.; Bowring, A.; McGehee, M.D. Towards enabling stable lead halide perovskite solar cells; interplay between structural, environmental, and thermal stability. *J. Mater. Chem. A* **2017**, *5*, 11483–11500. [[CrossRef](#)]
14. Xiao, J.W.; Liu, L.; Zhang, D.; De Marco, N.; Lee, J.W.; Lin, O.; Chen, Q.; Yang, Y. The Emergence of the Mixed Perovskites and Their Applications as Solar Cells. *Adv. Energy Mater.* **2017**, *7*, 1700491. [[CrossRef](#)]
15. Tai, Q.; You, P.; Sang, H.; Liu, Z.; Hu, C.; Chan, H.L.; Yan, F. Efficient and stable perovskite solar cells prepared in ambient air irrespective of the humidity. *Nat. Commun.* **2016**, *7*, 11105. [[CrossRef](#)] [[PubMed](#)]
16. Asuo, I.M.; Gedamu, D.; Doumon, N.Y.; Ka, I.; Pignolet, A.; Cloutier, S.G.; Nechache, R. Ambient condition-processing strategy for improved air-stability and efficiency in mixed-cation perovskite solar cells. *Mater. Adv.* **2020**, *1*, 1866–1876. [[CrossRef](#)]
17. Krishna, B.G.; Ghosh, D.S.; Tiwari, S. Progress in ambient air-processed perovskite solar cells: Insights into processing techniques and stability assessment. *Solar Energy* **2021**, *224*, 1369–1395. [[CrossRef](#)]
18. Gratzel, M. The Rise of Highly Efficient and Stable Perovskite Solar Cells. *Acc. Chem. Res.* **2017**, *50*, 487–491. [[CrossRef](#)]
19. Luo, P.; Zhou, S.; Zhou, Y.; Xia, W.; Sun, L.; Cheng, J.; Xu, C.; Lu, Y. Fabrication of Cs(x)FA(1-x)PbI(3) Mixed-Cation Perovskites via Gas-Phase-Assisted Compositional Modulation for Efficient and Stable Photovoltaic Devices. *ACS Appl. Mater. Interfaces* **2017**, *9*, 42708–42716. [[CrossRef](#)]
20. Cao, X.; Hao, L.; Liu, Z.; Su, G.; He, X.; Zeng, Q.; Wei, J. All green solvent engineering of organic-inorganic hybrid perovskite layer for high-performance solar cells. *Chem. Eng. J.* **2022**, *437*, 135458. [[CrossRef](#)]
21. Li, P.; Cheng, Y.; Zhou, L.; Yu, X.; Jiang, J.; He, M.; Liang, X.; Xiang, W. Photoluminescence properties and device application of CsPb<sub>2</sub>Br<sub>5</sub> quantum dots in glasses. *Mater. Res. Bull.* **2018**, *105*, 63–67. [[CrossRef](#)]
22. Wang, F.; Yu, H.; Xu, H.; Zhao, N. HPbI<sub>3</sub>: A New Precursor Compound for Highly Efficient Solution-Processed Perovskite Solar Cells. *Adv. Funct. Mater.* **2015**, *25*, 1120–1126. [[CrossRef](#)]
23. Li, G.; Zhang, T.; Guo, N.; Xu, F.; Qian, X.; Zhao, Y. Ion-Exchange-Induced 2D-3D Conversion of HMA(1-x)FA(x)PbI(3)Cl Perovskite into a High-Quality MA(1-x)FA(x)PbI(3) Perovskite. *Angew. Chem. Int. Ed. Engl.* **2016**, *55*, 13460–13464. [[CrossRef](#)]
24. Pool, V.L.; Dou, B.; Van Campen, D.G.; Klein-Stockert, T.R.; Barnes, F.S.; Shaheen, S.E.; Ahmad, M.I.; van Hest, M.F.; Toney, M.F. Thermal engineering of FAPbI(3) perovskite material via radiative thermal annealing and in situ XRD. *Nat. Commun.* **2017**, *8*, 14075. [[CrossRef](#)] [[PubMed](#)]
25. Liu, Y.; Yang, Z.; Cui, D.; Ren, X.; Sun, J.; Liu, X.; Zhang, J.; Wei, Q.; Fan, H.; Yu, F.; et al. Two-Inch-Sized Perovskite CH<sub>3</sub>NH<sub>3</sub>PbX<sub>3</sub> (X = Cl, Br, I) Crystals: Growth and Characterization. *Adv. Mater.* **2015**, *27*, 5176–5183. [[CrossRef](#)] [[PubMed](#)]
26. Li, Z.; Yang, M.; Park, J.-S.; Wei, S.-H.; Berry, J.J.; Zhu, K. Stabilizing Perovskite Structures by Tuning Tolerance Factor: Formation of Formamidinium and Cesium Lead Iodide Solid-State Alloys. *Chem. Mater.* **2015**, *28*, 284–292. [[CrossRef](#)]
27. Tang, X.; Han, S.; Zu, Z.; Hu, W.; Zhou, D.; Du, J.; Hu, Z.; Li, S.; Zang, Z. All-Inorganic Perovskite CsPb<sub>2</sub>Br<sub>5</sub> Microsheets for Photodetector Application. *Front. Phys.* **2018**, *5*, 69. [[CrossRef](#)]
28. Lee, J.-W.; Kim, D.-H.; Kim, H.-S.; Seo, S.-W.; Cho, S.M.; Park, N.-G. Formamidinium and Cesium Hybridization for Photo- and Moisture-Stable Perovskite Solar Cell. *Adv. Energy Mater.* **2015**, *5*, 1501310. [[CrossRef](#)]

29. Zhang, Z.; Zhu, Y.; Wang, W.; Zheng, W.; Lin, R.; Huang, F. Growth, characterization and optoelectronic applications of pure-phase large-area CsPb<sub>2</sub>Br<sub>5</sub> flake single crystals. *J. Mater. Chem. C* **2018**, *6*, 446–451. [[CrossRef](#)]
30. Peng, Z.; Wei, Q.; Chen, H.; Liu, Y.; Wang, F.; Jiang, X.; Liu, W.; Zhou, W.; Ling, S.; Ning, Z. Cs<sub>0.15</sub>FA<sub>0.85</sub>PbI<sub>3</sub>/Cs<sub>x</sub>FA<sub>1-x</sub>PbI<sub>3</sub> core/shell heterostructure for highly stable and efficient perovskite solar cells. *Cell Rep. Phys. Sci.* **2020**, *1*, 100224. [[CrossRef](#)]
31. Cheng, Y.; Xu, X.; Xie, Y.; Li, H.-W.; Qing, J.; Ma, C.; Lee, C.-S.; So, F.; Tsang, S.-W. 18% High-Efficiency Air-Processed Perovskite Solar Cells Made in a Humid Atmosphere of 70% RH. *Solar RRL* **2017**, *1*, 1700097. [[CrossRef](#)]
32. Wang, Z.; Zhou, Y.; Pang, S.; Xiao, Z.; Zhang, J.; Chai, W.; Xu, H.; Liu, Z.; Padture, N.P.; Cui, G. Additive-Modulated Evolution of HC(NH<sub>2</sub>)<sub>2</sub>PbI<sub>3</sub> Black Polymorph for Mesoscopic Perovskite Solar Cells. *Chem. Mater.* **2015**, *27*, 7149–7155. [[CrossRef](#)]
33. Kim, H.S.; Lee, C.R.; Im, J.H.; Lee, K.B.; Moehl, T.; Marchioro, A.; Moon, S.J.; Humphry-Baker, R.; Yum, J.H.; Moser, J.E.; et al. Lead iodide perovskite sensitized all-solid-state submicron thin film mesoscopic solar cell with efficiency exceeding 9%. *Sci. Rep.* **2012**, *2*, 591. [[CrossRef](#)]
34. Wang, Y.; Zhao, Y.; Gao, F.; Chen, H.; Chen, Y.; Wang, X.; Liu, X.; Zhu, K. Sequential Cesium Incorporation for Highly Efficient Formamidinium-Cesium Perovskite Solar Cells. *Chem* **2022**. [[CrossRef](#)]
35. Lindblad, R.; Jena, N.K.; Philippe, B.; Oscarsson, J.; Bi, D.; Lindblad, A.; Mandal, S.; Pal, B.; Sarma, D.D.; Karis, O.; et al. Electronic Structure of CH<sub>3</sub>NH<sub>3</sub>PbX<sub>3</sub> Perovskites: Dependence on the Halide Moiety. *J. Phys. Chem. C* **2015**, *119*, 1818–1825. [[CrossRef](#)]
36. Ren, L.; Gao, K.; Tan, Q.; Qing, C.; Wang, Q.; Yang, P.; Liu, Y. High-performance perovskite photodetectors based on CsPbBr<sub>3</sub> microwire arrays. *Appl. Opt.* **2021**, *60*, 8896–8903. [[CrossRef](#)]
37. Chen, G.; Yu, Y.; Zheng, K.; Ding, T.; Wang, W.; Jiang, Y.; Yang, Q. Fabrication of Ultrathin Bi<sub>2</sub>S<sub>3</sub> Nanosheets for High-Performance, Flexible, Visible-NIR Photodetectors. *Small* **2015**, *11*, 2848–2855. [[CrossRef](#)]
38. Tian, W.; Min, L.; Cao, F.; Li, L. Nested Inverse Opal Perovskite toward Superior Flexible and Self-Powered Photodetection Performance. *Adv. Mater.* **2020**, *32*, 1906974. [[CrossRef](#)]
39. Bao, C.; Yang, J.; Bai, S.; Xu, W.; Yan, Z.; Xu, Q.; Liu, J.; Zhang, W.; Gao, F. High performance and stable all-inorganic metal halide perovskite-based photodetectors for optical communication applications. *Adv. Mater.* **2018**, *30*, 1803422. [[CrossRef](#)]
40. Eze, V.O.; Adams, G.R.; Braga Carani, L.; Simpson, R.J.; Okoli, O.I. Enhanced inorganic CsPbI<sub>2</sub>Br<sub>2</sub> perovskite film for a sensitive and rapid response self-powered photodetector. *J. Phys. Chem. C* **2020**, *124*, 20643–20653. [[CrossRef](#)]
41. Li, D.; Zhou, D.; Xu, W.; Chen, X.; Pan, G.; Zhou, X.; Ding, N.; Song, H. Plasmonic photonic crystals induced two-order fluorescence enhancement of blue perovskite nanocrystals and its application for high-performance flexible ultraviolet photodetectors. *Adv. Funct. Mater.* **2018**, *28*, 1804429. [[CrossRef](#)]
42. Wang, T.; Zheng, D.; Zhang, J.; Qiao, J.; Min, C.; Yuan, X.; Somekh, M.; Feng, F. High-Performance and Stable Plasmonic-Functionalized Formamidinium-Based Quasi-2D Perovskite Photodetector for Potential Application in Optical Communication. *Adv. Funct. Mater.* **2022**, *32*, 2208694. [[CrossRef](#)]
43. Yun, Y.; Han, G.S.; Park, G.N.; Kim, J.; Park, J.; Vidyasagar, D.; Jung, J.; Choi, W.C.; Choi, Y.J.; Heo, K. A Wide Bandgap Halide Perovskite Based Self-Powered Blue Photodetector with 84.9% of External Quantum Efficiency. *Adv. Mater.* **2022**, *34*, 2206932. [[CrossRef](#)]
44. Cheng, W.; He, X.; Wang, J.G.; Tian, W.; Li, L. N-(2-aminoethyl) Acetamide Additive Enables Phase-Pure and Stable α-FAPbI<sub>3</sub> for Efficient Self-Powered Photodetectors. *Adv. Mater.* **2022**, *34*, 2208325. [[CrossRef](#)] [[PubMed](#)]
45. Adams, G.R.; Eze, V.O.; Shohag, M.A.S.; Simpson, R.; Parker, H.; Okoli, O.I. Fabrication of rapid response self-powered photodetector using solution-processed triple cation lead-halide perovskite. *Eng. Res. Express* **2020**, *2*, 015043. [[CrossRef](#)]
46. Vuong, V.-H.; Pammi, S.; Ippili, S.; Jella, V.; Thi, T.N.; Pasupuleti, K.S.; Kim, M.-D.; Jeong, M.J.; Jeong, J.-R.; Chang, H.S. Flexible, Stable, and Self-Powered Photodetectors Embedded with Chemical Vapor Deposited Lead-Free Bismuth Mixed Halide Perovskite Films. *Chem. Eng. J.* **2023**, *458*, 141473. [[CrossRef](#)]
47. Pasupuleti, K.S.; Chougule, S.S.; Jung, N.; Yu, Y.-J.; Oh, J.-E.; Kim, M.-D. Plasmonic Pt nanoparticles triggered efficient charge separation in TiO<sub>2</sub>/GaN NRs hybrid heterojunction for the high performance self-powered UV photodetectors. *Appl. Surf. Sci.* **2022**, *594*, 153474. [[CrossRef](#)]
48. Meng, J.; Li, Q.; Huang, J.; Pan, C.; Li, Z. Self-powered photodetector for ultralow power density UV sensing. *Nano Today* **2022**, *43*, 101399. [[CrossRef](#)]
49. Lin, D.; Shi, T.; Xie, H.; Wan, F.; Ren, X.; Liu, K.; Zhao, Y.; Ke, L.; Lin, Y.; Gao, Y.; et al. Ion Migration Accelerated Reaction between Oxygen and Metal Halide Perovskites in Light and Its Suppression by Cesium Incorporation. *Adv. Energy Mater.* **2021**, *11*, 2002552. [[CrossRef](#)]
50. Niu, G.; Li, W.; Meng, F.; Wang, L.; Dong, H.; Qiu, Y. Study on the stability of CH<sub>3</sub>NH<sub>3</sub>PbI<sub>3</sub> films and the effect of post-modification by aluminum oxide in all-solid-state hybrid solar cells. *J. Mater. Chem. A* **2014**, *2*, 705–710. [[CrossRef](#)]
51. Chen, Y.; Yang, X.; Liu, P.; Wang, W.; Ran, R.; Zhou, W.; Shao, Z. Improving Moisture/Thermal Stability and Efficiency of CH<sub>3</sub>NH<sub>3</sub>PbI<sub>3</sub>-Based Perovskite Solar Cells via Gentle Butyl Acrylate Additive Strategy. *Solar RRL* **2020**, *5*, 2000621. [[CrossRef](#)]
52. Liu, X.; Ren, S.; Li, Z.; Guo, J.; Yi, S.; Yang, Z.; Hao, W.; Li, R.; Zhao, J. Flexible transparent high-efficiency photoelectric perovskite resistive switching memory. *Adv. Funct. Mater.* **2022**, *32*, 2202951. [[CrossRef](#)]
53. Yuan, Y.; Huang, J. Ion Migration in Organometal Trihalide Perovskite and Its Impact on Photovoltaic Efficiency and Stability. *Acc. Chem. Res.* **2016**, *49*, 286–293. [[CrossRef](#)]
54. Yan, X.; Fan, W.; Cheng, F.; Sun, H.; Xu, C.; Wang, L.; Kang, Z.; Zhang, Y. Ion migration in hybrid perovskites: Classification, identification, and manipulation. *Nano Today* **2022**, *44*, 101503. [[CrossRef](#)]

55. Doherty, T.A.; Nagane, S.; Kubicki, D.J.; Jung, Y.-K.; Johnstone, D.N.; Iqbal, A.N.; Guo, D.; Frohna, K.; Danaie, M.; Tennyson, E.M. Stabilized tilted-octahedra halide perovskites inhibit local formation of performance-limiting phases. *Science* **2021**, *374*, 1598–1605. [[CrossRef](#)] [[PubMed](#)]
56. Nan, Z.-A.; Chen, L.; Liu, Q.; Wang, S.-H.; Chen, Z.-X.; Kang, S.-Y.; Ji, J.-B.; Tan, Y.-Y.; Hui, Y.; Yan, J.-W.; et al. Revealing phase evolution mechanism for stabilizing formamidinium-based lead halide perovskites by a key intermediate phase. *Chem* **2021**, *7*, 2513–2526. [[CrossRef](#)]
57. Cheng, Y.; Ding, L. Pushing commercialization of perovskite solar cells by improving their intrinsic stability. *Energy Environ. Sci.* **2021**, *14*, 3233–3255. [[CrossRef](#)]
58. Li, B.; Jiao, Y.; Qin, S.; Wang, Y.; Liu, H.; Li, R.; Hao, W.; Li, H.; Xia, Y.; Li, X. Photoinduced Strain in Organometal Halide Perovskites. *J. Phys. Chem. Lett.* **2023**, *14*, 1343–1353. [[CrossRef](#)]
59. Liu, D.; Liu, F.; Liu, Y.; Pang, Z.; Zhuang, X.; Yin, Y.; Dong, S.; He, L.; Tan, Y.; Liao, L. Schottky-Contacted High-Performance GaSb Nanowires Photodetectors Enabled by Lead-Free All-Inorganic Perovskites Decoration. *Small* **2022**, *18*, 2200415. [[CrossRef](#)]
60. Xia, G.; Huang, B.; Zhang, Y.; Zhao, X.; Wang, C.; Jia, C.; Zhao, J.; Chen, W.; Li, J. Nanoscale Insights into Photovoltaic Hysteresis in Triple-Cation Mixed-Halide Perovskite: Resolving the Role of Polarization and Ionic Migration. *Adv. Mater.* **2019**, *31*, 1902870. [[CrossRef](#)]
61. Cacovich, S.; Cina, L.; Matteocci, F.; Divitini, G.; Midgley, P.A.; Di Carlo, A.; Ducati, C. Gold and iodine diffusion in large area perovskite solar cells under illumination. *Nanoscale* **2017**, *9*, 4700–4706. [[CrossRef](#)]
62. Shlenskaya Natalia, N.; Belich, N.A.; Grätzel, M.; Goodilin, E.A.; Tarasov, A.B. Light-induced reactivity of gold and hybrid perovskite as a new possible degradation mechanism in perovskite solar cells. *J. Mater. Chem. A* **2018**, *6*, 1780–1786. [[CrossRef](#)]
63. Jacobsson, T.J.; Schwan, L.J.; Ottosson, M.; Hagfeldt, A.; Edvinsson, T. Determination of Thermal Expansion Coefficients and Locating the Temperature-Induced Phase Transition in Methylammonium Lead Perovskites Using X-ray Diffraction. *Inorg. Chem.* **2015**, *54*, 10678–10685. [[CrossRef](#)] [[PubMed](#)]
64. Gratia, P.; Grancini, G.; Audinot, J.N.; Jeanbourquin, X.; Mosconi, E.; Zimmermann, I.; Dowsett, D.; Lee, Y.; Gratzel, M.; De Angelis, F.; et al. Intrinsic Halide Segregation at Nanometer Scale Determines the High Efficiency of Mixed Cation/Mixed Halide Perovskite Solar Cells. *J. Am. Chem. Soc.* **2016**, *138*, 15821–15824. [[CrossRef](#)] [[PubMed](#)]
65. Philippe, B.; Saliba, M.; Correa-Baena, J.-P.; Cappel, U.B.; Turren-Cruz, S.-H.; Grätzel, M.; Hagfeldt, A.; Rensmo, H. Chemical Distribution of Multiple Cation (Rb<sup>+</sup>, Cs<sup>+</sup>, MA<sup>+</sup>, and FA<sup>+</sup>) Perovskite Materials by Photoelectron Spectroscopy. *Chem. Mater.* **2017**, *29*, 3589–3596. [[CrossRef](#)]
66. Zhu, C.; Niu, X.; Fu, Y.; Li, N.; Hu, C.; Chen, Y.; He, X.; Na, G.; Liu, P.; Zai, H.; et al. Strain engineering in perovskite solar cells and its impacts on carrier dynamics. *Nat. Commun.* **2019**, *10*, 815. [[CrossRef](#)] [[PubMed](#)]
67. Abdi-Jalebi, M.; Andaji-Garmaroudi, Z.; Cacovich, S.; Stavrakas, C.; Philippe, B.; Richter, J.M.; Alsari, M.; Booker, E.P.; Hutter, E.M.; Pearson, A.J.; et al. Maximizing and stabilizing luminescence from halide perovskites with potassium passivation. *Nature* **2018**, *555*, 497–501. [[CrossRef](#)]
68. Brennan, M.C.; Draguta, S.; Kamat, P.V.; Kuno, M. Light-Induced Anion Phase Segregation in Mixed Halide Perovskites. *ACS Energy Lett.* **2017**, *3*, 204–213. [[CrossRef](#)]
69. Bush, K.A.; Rolston, N.; Gold-Parker, A.; Manzoor, S.; Hausele, J.; Yu, Z.J.; Raiford, J.A.; Checharoen, R.; Holman, Z.C.; Toney, M.F.; et al. Controlling Thin-Film Stress and Wrinkling during Perovskite Film Formation. *ACS Energy Lett.* **2018**, *3*, 1225–1232. [[CrossRef](#)]
70. Zheng, X.; Wu, C.; Jha, S.K.; Li, Z.; Zhu, K.; Priya, S. Improved Phase Stability of Formamidinium Lead Triiodide Perovskite by Strain Relaxation. *ACS Energy Lett.* **2016**, *1*, 1014–1020. [[CrossRef](#)]
71. Prasanna, R.; Gold-Parker, A.; Leijtens, T.; Conings, B.; Babayigit, A.; Boyen, H.G.; Toney, M.F.; McGehee, M.D. Band Gap Tuning via Lattice Contraction and Octahedral Tilting in Perovskite Materials for Photovoltaics. *J. Am. Chem. Soc.* **2017**, *139*, 11117–11124. [[CrossRef](#)] [[PubMed](#)]
72. Murali, B.; Yengel, E.; Peng, W.; Chen, Z.; Alias, M.S.; Alarousu, E.; Ooi, B.S.; Burlakov, V.; Goriely, A.; Eddaoudi, M.; et al. Temperature-Induced Lattice Relaxation of Perovskite Crystal Enhances Optoelectronic Properties and Solar Cell Performance. *J. Phys. Chem. Lett.* **2017**, *8*, 137–143. [[CrossRef](#)] [[PubMed](#)]
73. McMeekin, D.P.; Wang, Z.; Rehman, W.; Pulvirenti, F.; Patel, J.B.; Noel, N.K.; Johnston, M.B.; Marder, S.R.; Herz, L.M.; Snaith, H.J. Crystallization Kinetics and Morphology Control of Formamidinium-Cesium Mixed-Cation Lead Mixed-Halide Perovskite via Tunability of the Colloidal Precursor Solution. *Adv. Mater.* **2017**, *29*, 1607039. [[CrossRef](#)] [[PubMed](#)]

**Disclaimer/Publisher's Note:** The statements, opinions and data contained in all publications are solely those of the individual author(s) and contributor(s) and not of MDPI and/or the editor(s). MDPI and/or the editor(s) disclaim responsibility for any injury to people or property resulting from any ideas, methods, instructions or products referred to in the content.